

Observations of Near-Surface Vertical Wind Profiles and Vertical Momentum Fluxes from VORTEX-SE 2017: Comparisons to Monin–Obukhov Similarity Theory

PAUL M. MARKOWSKI AND NATHAN T. LIS^a

*Department of Meteorology and Atmospheric Science, The Pennsylvania State University,
University Park, Pennsylvania*

DAVID D. TURNER

NOAA/OAR/ESRL/Global Systems Division, Boulder, Colorado

TEMPLE R. LEE AND MICHAEL S. BUBAN

*Cooperative Institute for Mesoscale Meteorological Studies, Norman, Oklahoma, and NOAA/Air Resources
Laboratory/Atmospheric Turbulence and Diffusion Division, Oak Ridge, Tennessee*

(Manuscript received 26 March 2019, in final form 31 July 2019)

ABSTRACT

Observations of near-surface vertical wind profiles and vertical momentum fluxes obtained from a Doppler lidar and instrumented towers deployed during VORTEX-SE in the spring of 2017 are analyzed. In particular, departures from the predictions of Monin–Obukhov similarity theory (MOST) are documented on thunderstorm days, both in the warm air masses ahead of storms and within the cool outflow of storms, where MOST assumptions (e.g., horizontal homogeneity and a steady state) are least credible. In these regions, it is found that the nondimensional vertical wind shear near the surface commonly exceeds predictions by MOST. The departures from MOST have implications for the specification of the lower boundary condition in numerical simulations of convective storms. Documenting departures from MOST is a necessary first-step toward improving the lower boundary condition and parameterization of near-surface turbulence (“wall models”) in storm simulations.

1. Introduction

The inclusion of surface momentum fluxes in idealized, “research-driven” convective storm simulations (i.e., simulations not done in the interest of numerical weather prediction, but rather controlled simulations designed to study physical processes within storms) is becoming increasingly common, owing to the increased model resolution and interest in boosting the realism of the simulations as computing power increases (Adlerman et al. 1999; Adlerman and Droegemeier 2002; Schenkman et al. 2012, 2014, 2016; Markowski 2016; Mashiko 2016; Roberts et al. 2016; Orf et al. 2017;

Coffer and Parker 2017, 2018; Yokota et al. 2018). Several investigators have found that the inclusion of surface drag can alter the evolution and even the dynamics of storms in important ways (Schenkman et al. 2012, 2014; Markowski 2016; Roberts et al. 2016). Some research-driven simulations of convective storms also have included surface heat and moisture fluxes (Frame and Markowski 2010, 2013; Schenkman et al. 2012, 2014; Oberthaler and Markowski 2013; Nowotarski et al. 2014, 2015; Nowotarski and Markowski 2016). Although this has been less common, it is safe to assume the inclusion of surface heat and moisture fluxes will become more commonplace in the future. In operational simulations (i.e., those performed for numerical weather prediction), surface fluxes have always been included. However, as resolution increases and convection-allowing models are increasingly relied upon (e.g., “Warn-on-Forecast”; Stensrud et al. 2009; Lawson et al. 2018), it will likely become increasingly important to consider

^aCurrent affiliation: School of Meteorology, University of Oklahoma, Norman, Oklahoma.

Corresponding author: Paul M. Markowski, pmarkowski@psu.edu

whether surface flux parameterizations are up to the task, especially given the well-known sensitivity of convective storms to the near-surface thermodynamic and vertical wind profiles (e.g., Markowski and Richardson 2014; Coffey and Parker 2015, 2017, 2018; Coffey et al. 2017).

The Monin–Obukhov similarity theory (MOST) of the atmospheric surface layer (Monin and Obukhov 1954) has been the standard framework by which surface fluxes of momentum, heat, and moisture are parameterized in numerical simulations (Foken 2006; Wilson 2008). MOST relates the vertical profiles of nondimensional mean flow and turbulence properties to a dimensionless height parameter z/L , where z is the height above the surface and L is the Obukhov length, which itself depends on the surface heat and momentum fluxes. Steadiness and horizontal homogeneity, which are the assumptions underpinning MOST, are unlikely to be satisfied within the downdrafts and outflow of convective storms, especially in strongly curved flow such as near an intensifying vortex, or in the vicinity of a gust front. These assumptions may not even be met within the near-storm environment, especially within boundary layers in which winds are rapidly accelerating toward a storm updraft or in boundary layers within complex terrain.

This article is about the characteristics of vertical wind profiles within the surface layer, both near and within convective storms, and their departures from MOST. We analyze data obtained from a Doppler lidar and instrumented towers deployed during the Verification of the Origins of Rotation in Tornadoes Experiment–Southeast (VORTEX-SE) field campaign during the spring of 2017. We are in desperate need of near-surface wind observations—and knowledge of their departures from MOST—in order to assess the credibility of present-day convective storm simulations and to develop/evaluate new formulations for the lower boundary condition in future simulations. Despite the fact that MOST has been the “industry standard” for over half a century, deviations from it are still not well understood, especially within convective storms. A priori, one might expect potentially large departures at times when surface winds are unsteady and/or being subjected to large horizontal pressure-gradient forces. Documenting departures from MOST is a necessary first step toward improving the lower boundary condition and parameterization of near-surface turbulence (“wall models”).

In section 2, additional details are provided about the data that are analyzed, as well as the analysis methods. Sections 3 and 4 contain, respectively, the results and discussion. Concluding remarks are provided in section 5.

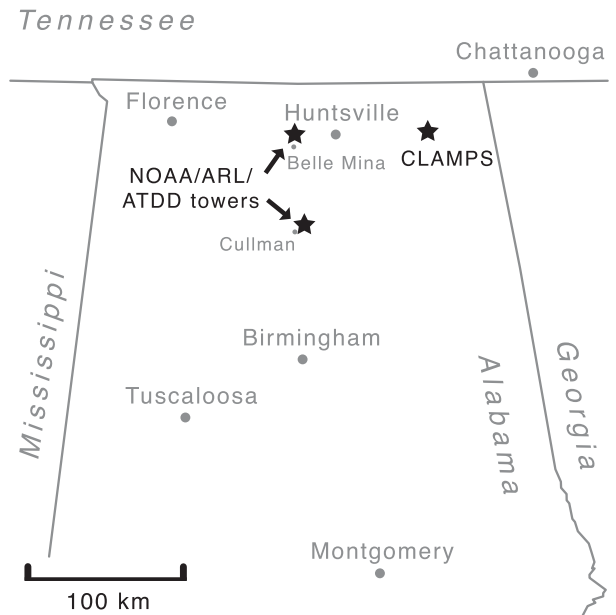


FIG. 1. Locations of CLAMPS and the NOAA/ARL/ATDD towers during the VORTEX-SE field campaign during the spring of 2017.

2. Data and methodology

a. Vertical wind profile observations from CLAMPS

The Collaborative Lower Atmospheric Mobile Profiling System (CLAMPS; Wagner et al. 2019), which includes a Halo Streamline Doppler lidar (Pearson et al. 2009), was deployed at the Scottsboro Airport in north-central Alabama in March and April 2017 in support of the VORTEX-SE field campaign (Fig. 1; Turner 2017). The Doppler lidar measured radial winds at a 60° elevation angle and at 8 evenly spaced azimuths (at 1-s integration times per angle), followed by a series of 1-s vertical stares. The plan position indicator (PPI) scans were analyzed using the velocity–azimuth display (VAD) technique to derive the horizontal winds. Vertical profiles of horizontal winds were retrieved from the lidar at 182-s intervals and every 26 m AGL, starting at 13 m AGL.¹ Data from the lowest two levels (13 and 39 m AGL) were excluded from analysis owing to poor data quality. An anemometer was collocated with CLAMPS, measuring wind every 5 s at a height of approximately 5.7 m AGL (Turner 2018). The airport is situated in a region characterized by hills, deciduous woodlands, and some fields used for agriculture (the area

¹ CLAMPS was also deployed in the spring of 2016, but data from 2016 were excluded from the analysis owing to the coarser vertical resolution of the 2016 wind profiles.

TABLE 1. VORTEX-SE operations days in spring 2017.

Intensive observing period (IOP)	Date	Description
1A	25 Mar	Weak convective line
1B	27 Mar	Severe (nontornadic) convection
2	30 Mar	No convection
3A	3 Apr	No convection (stratiform rain from a convective system to the south overspread northern AL in the predawn hours)
3B	5 Apr	Weak supercellular convection
4A	26 Apr	Dissipating convective system after midnight
4B	28 Apr	No convection
4C	30 Apr	Tornadic convective system

in the immediate vicinity of the airport is largely devoid of trees).

Vertical wind profiles were binned by weather regime. The weather regimes are as follows: 1) fair-weather, nonoperations days; 2) VORTEX-SE operations days, but before the arrival of cool outflow from convective storms (i.e., in what might be regarded as “fair weather,” but this regime differs from the first regime in that a strong horizontal pressure-gradient force and geostrophic vertical wind shear are frequently present on VORTEX-SE operations days, so there might be an a priori expectation that MOST would not be as applicable); and 3) VORTEX-SE operations days, within the outflow of convective storms (such regions are characterized by large horizontal heterogeneity and unsteadiness, especially in the vicinity of gust fronts). The VORTEX-SE operations days are listed in Table 1. In the “warm sector” regimes (i.e., regimes 1 and 2), vertical profiles of the magnitude of the mean horizontal wind vector, hereafter referred to as the mean wind speed \bar{u} , were obtained over 30-min intervals. Although it is perhaps more conventional in the boundary layer community to deal with the mean wind speed, the horizontal wind vector was averaged instead. This approach was adopted because vertical shear is the focus of this study, and the vertical shear of the mean speed can be up to a few percent too large, depending on the variance of the lateral wind speed variations (see section 2b of Businger et al. 1971). In the outflow regime (i.e., regime 3), 15-min averages were used owing to considerable horizontal heterogeneity within the outflow. Even 15-min averages are quite possibly too long, but it is unclear what averaging period is ideal. Anemometer velocity data were averaged over the same intervals as the lidar-derived wind profiles. The arrival of outflow was identified by a sudden drop in temperature at the CLAMPS location; a wind shift also typically accompanied the passage of the outflow boundaries. Given the well-known limitations of MOST in nocturnal boundary layers (e.g., Mahrt 1998, 1999,

2010, 2014; Optis et al. 2014; Gibbs et al. 2015), only data obtained between 1500 and 2300 UTC were included in this study.

For each mean wind profile, profiles of non-dimensional mean wind \bar{u}/u_* , and nondimensional mean wind shear,

$$\phi_m = \frac{kz}{u_*} \frac{\partial \bar{u}}{\partial z}, \quad (1)$$

were computed, where u_* is the friction velocity and k is the von Kármán constant, which is taken to be 0.40. Centered-in-space finite-difference approximations for $\partial \bar{u}/\partial z$ are used, except at the first lidar level, where a second-order, one-sided finite-difference formula for $\partial \bar{u}/\partial z$ based on the 65, 91, and 117 m winds is used (this was preferable to using the anemometer data, given the large gap between the anemometer height and lowest usable lidar gate, and especially large nonlinearity in the wind profile in that layer).

The friction velocity was computed from the mean wind speed at anemometer level (\bar{u}_a) and an assumed roughness length (z_0) via

$$u_* = \frac{\bar{u}_a k}{\ln(z_a/z_0)}, \quad (2)$$

where z_a is the height of the anemometer. No static stability corrections were included in the u_* calculation because no proximate surface heat flux data were available. A roughness length of 0.15 m was used. The value was settled upon after evaluating a range of roughness lengths ranging from 0.01 to 0.30 m. Roughness lengths of 0.10–0.20 m result in profiles of \bar{u}/u_* and ϕ_m , that agree well with MOST predictions on fair-weather, nonoperations days (Figs. 2b,c) (although the surface heat flux was unknown, it is safe to assume that it generally would have been positive during the daytime).

Calculations of \bar{u}/u_* and ϕ_m are compared against MOST predictions of \bar{u}/u_* and ϕ_m in section 3.

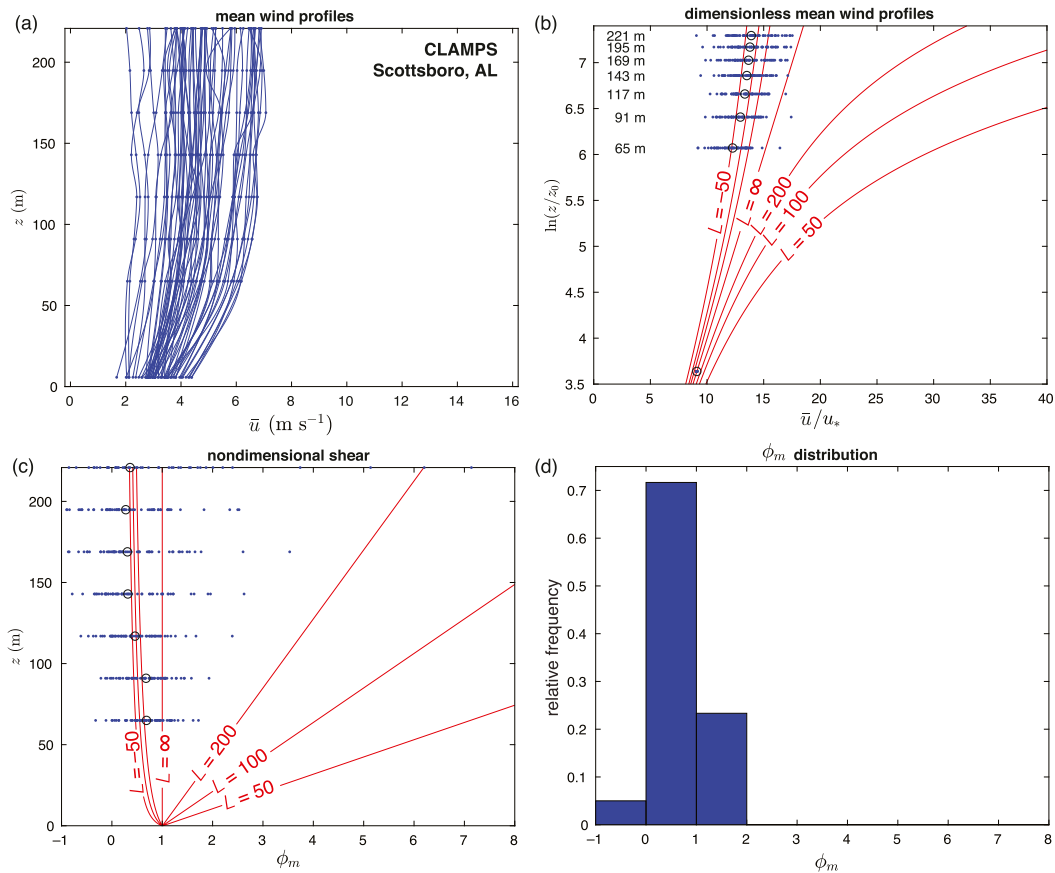


FIG. 2. (a) Mean wind speeds (\bar{u}) observed by CLAMPS on fair weather days during the spring 2017 VORTEX-SE field phase. (b) Nondimensional wind speed, \bar{u}/u_* , as a function of nondimensional height, $\ln(z/z_0)$. (c) Nondimensional shear ϕ_m as a function of height. In (b),(c), the unfilled circles indicate means at each altitude, and the red curves are MOST predictions for Obukhov lengths L of ± 50 , 100, 200 m, and ∞ . (d) Histogram of ϕ_m values at $z = 65$ m and $z = 91$ m (altitudes that can be assured to be within the surface layer). The reason $\bar{u}/u_* = \text{constant} = 9.1$ for the first (lowest) data point in (b) is because this represents the anemometer wind, which is also used to diagnose u_* ; from (2), $\bar{u}_a/u_* = k^{-1}\ln(z_a/z_0) = 9.1$.

The MOST-predicted nondimensional velocity profiles are obtained by integrating (1), that is, $\bar{u}/u_* = k^{-1}\int_{z_0}^z \phi_m d\ln z$, where $\phi_m = (1 - 15z/L)^{-1/4}$ for an unstable or neutral surface layer, and $\phi_m = 1 + 4.7z/L$ for a stable surface layer. The functions for ϕ_m are those of Businger et al. (1971) and are applicable in the range $-2 < z/L < 1$. Other functions have been proposed (e.g., Höglström 1988), but are qualitatively similar to the Businger et al. formulation.

The sensitivity of the u_* calculations to the z_0 specification is examined in the appendix, as are the errors in calculations of \bar{u}/u_* and ϕ_m . In addition to the omission of a static stability correction in (2), another limitation is that (2) itself comes from MOST, and its use in subsequent calculations of \bar{u}/u_* and ϕ_m in regimes 2 and 3 (i.e., regimes for which the assumptions underpinning MOST might be questionable) is potentially problematic. However, it will be shown in section 2b that the use

of (2) to obtain u_* is not as limiting as it might seem, based on comparisons with u_* values obtained from eddy covariance observations obtained from a pair of instrumented towers.

b. Near-surface velocity and flux observations from the NOAA/ARL/ATDD towers

Two 10-m NOAA/ARL/ATDD (NOAA Air Resources Laboratory, Atmospheric Turbulence and Diffusion Division) micrometeorological towers (Lee et al. 2017, 2019) were installed during VORTEX-SE (Fig. 1). One tower was approximately 2 km north of Belle Mina at the Tennessee Valley Research and Extension Center. The other was installed near Cullman at the Auburn University North Alabama Horticulture Research Center. Both towers were situated in fairly flat terrain. The Belle Mina tower was surrounded by grazed pasture, whereas the Cullman tower was surrounded by

ungrazed pasture. We refer the reader to Lee et al. (2019) and Lee and Buban (2019, manuscript submitted to *J. Appl. Meteor. Climatol.*) for additional details on the sites' characteristics. Wind, temperature, and turbulent fluxes were measured at 3 m AGL and 10 m AGL. Turbulent fluxes were obtained from sonic anemometer data; mean winds were obtained from a propeller anemometer. As was the case for the CLAMPS Doppler lidar data, 30-min averaging periods were used in the fair-weather and prestorm weather regimes (regimes 1 and 2), and 15-min averaging periods were used within convective storm outflow (regime 3).

Eddy covariance observations were used to compute u_* via

$$u_* = [(\overline{u'w'})^2 + (\overline{v'w'})^2]^{1/4}, \quad (3)$$

where $\overline{u'w'}$ and $\overline{v'w'}$ are the streamwise and crosswise vertical momentum fluxes, respectively. Additional details about the data processing techniques used to compute the fluxes appear in Lee et al. (2019). The nondimensional shear at 6.5 m AGL (i.e., halfway between the 3 and 10 m AGL probes, where the centered difference approximation for $\partial\bar{u}/\partial z$ is valid) was computed via (1) by differencing the 3 and 10 m AGL mean winds and using the average u_* obtained at the two levels. Although ϕ_m was obtained at only a single level, the ϕ_m calculations relied on a measured value of u_* as opposed to a MOST-based diagnosis of u_* . The latter relied not only on the validity of MOST, but also required an assumed roughness length. As is also the case for the CLAMPS Doppler lidar data, only the 1500–2300 UTC period was analyzed.

One question raised in section 2a was whether estimates of u_* from \bar{u}_a , an estimated z_0 , and the MOST-based formulation for u_* given by (2) are good enough to use in the Doppler lidar-derived diagnoses of \bar{u}/u_* and ϕ_m that are presented in section 3. Figure 3 reveals that u_* values obtained from the tower mean wind observations via (2) generally agree well with u_* values obtained from tower eddy covariance observations via (3). Roughness lengths at the two tower locations were obtained from a least squares best fit of MOST-based u_* values to the tower-based u_* values. This fitting included Byun's (1990) stability corrections to u_* using the tower observations of L (Figs. 4b,d,f), which were obtained from each tower's u_* and heat flux observations (Figs. 4a,c,e) via

$$L = -\frac{\bar{\theta}_v u_*^3}{kgw'\theta'_v|_0}, \quad (4)$$

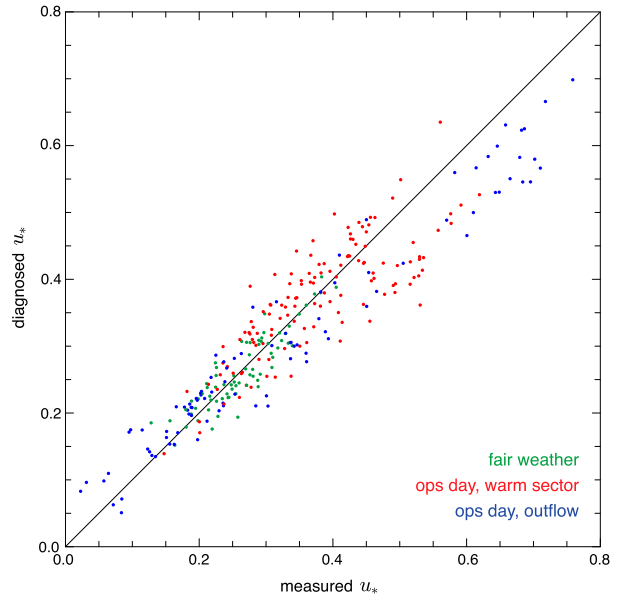


FIG. 3. Friction velocity (m s^{-1}) derived from NOAA/ARL/ATDD tower observations of vertical momentum fluxes at 3 m AGL (“measured u_* ”) vs friction velocity diagnosed from MOST using tower observations of 3-m wind speed (“diagnosed u_* ”).

where $\overline{w'\theta'_v}|_0$ is the kinematic flux of virtual potential temperature and $\bar{\theta}_v$ is the mean virtual potential temperature. The roughness lengths obtained for the tower locations at Belle Mina and Cullman are, respectively, 0.01 and 0.04 m. These roughness lengths were subsequently used with the expression in (2) to obtain the MOST-based u_* values without a static stability correction that are compared to the tower-based u_* values in Fig. 3. The rms difference between the two u_* values, which can be interpreted as the uncertainty in the MOST-based u_* values, is 0.05 m s^{-1} . The largest differences are in convective storm outflow, where the MOST-based u_* calculations might be compromised by unsteadiness, horizontal heterogeneity, and/or the unaccounted effects of stratification. The largest differences between the two u_* values rarely exceed 0.10 m s^{-1} . A more detailed error analysis appears in the appendix.

3. Results

a. Fair-weather days

On fair-weather, nonoperations days—that is, days generally characterized by weak synoptic-scale pressure gradients, baroclinicity, and geostrophic wind shear—vertical mean wind profiles retrieved from the CLAMPS Doppler lidar in the surface layer generally adhere to MOST expectations (Fig. 2). This is unsurprising,

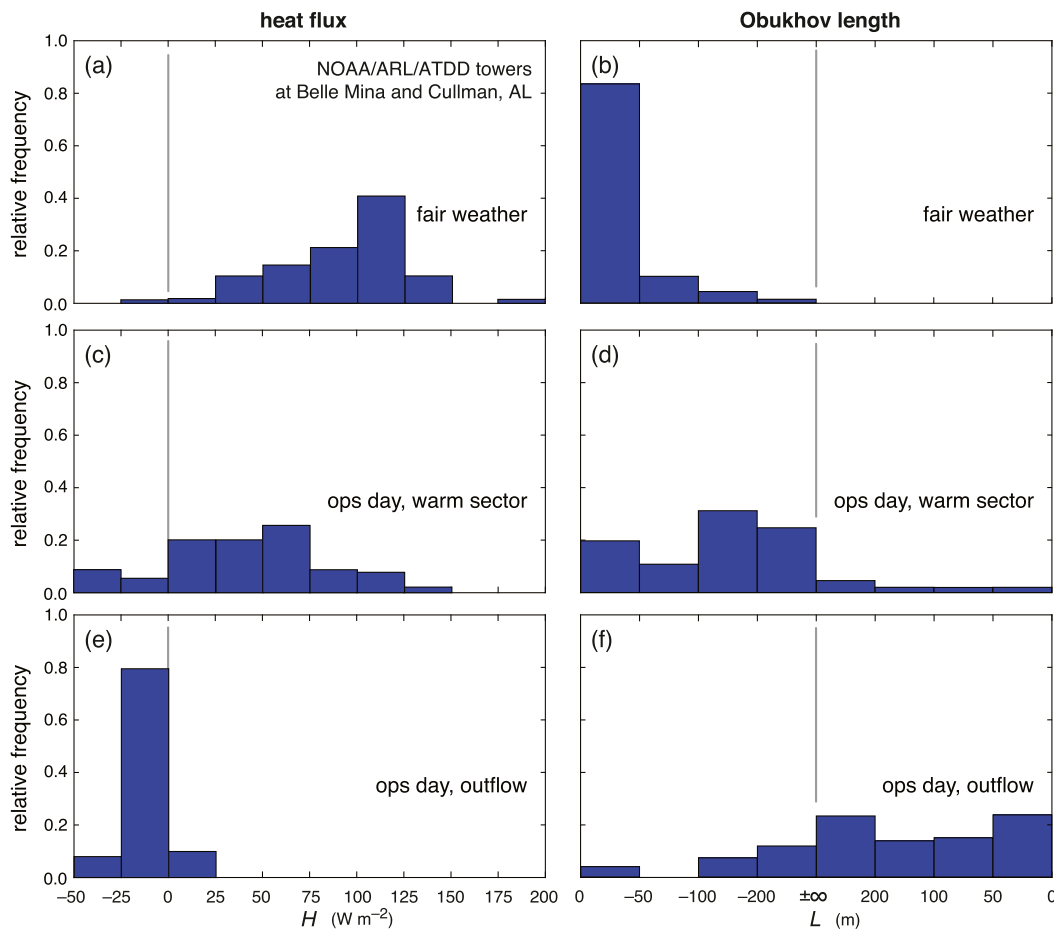


FIG. 4. Histograms of (a),(c),(e) surface heat flux H and (b),(d),(f) Obukhov length L diagnosed for the various weather regimes from the NOAA/ARL/ATDD tower observations (3 and 10 m AGL measurements were averaged).

especially given that the roughness length was tuned in order to obtain good agreement between the wind profiles and MOST predictions on fair-weather days.

The surface layer can be assumed to be 100–150 m deep at the times corresponding to the wind profiles depicted in Fig. 2, based on boundary layer depths of 1000–1500 m evident from nearby observed or model soundings. In Figs. 2b and 2c, which display \bar{u}/u_* and ϕ_m , respectively, the series of red curves that are overlaid represent MOST predictions of \bar{u}/u_* and ϕ_m for a range of L values. The diagonal line in Fig. 2b for $L = \infty$ has a slope of k , which corresponds to the well-known logarithmic wind profile that MOST predicts in a neutral surface layer. Nondimensional velocity \bar{u}/u_* generally increases with height at a rate less than k , which implies surface layers that are, on average, at least weakly unstable—a result that is unsurprising during the daytime hours in early spring and in agreement with surface heat flux data at the locations of the two NOAA/ARL/ATDD towers (Figs. 4a,b).

Values of ϕ_m most often lie in the 0.5–1.0 range within the surface layer, also in general agreement with MOST predictions (Figs. 2c,d). More than 70% of the ϕ_m values computed at heights of 65 and 91 m (heights that can be safely assumed to be within the surface layer) fall in the $\phi_m = 0$ –1 bin in the histogram shown in Fig. 2d, and of the small fraction in the $\phi_m = 1$ –2 bin, 80% have ϕ_m in the 1.0–1.3 range (Fig. 2c). It is unrealistic to expect every wind profile to conform to MOST predictions, even on fair-weather days, given the local heterogeneity in the surface characteristics at the CLAMPS site, in addition to uncertainties in the most appropriate averaging period (Pan and Patton 2017) and occasionally large errors in computed \bar{u}/u_* and ϕ_m . Error magnitude depends in part on the meteorological conditions, but typical errors in these two dimensionless quantities obtained from the CLAMP Doppler lidar observations are 0.7–2.0 and 0.4–0.8, respectively, based on the analysis in the appendix. The mean characteristics of the wind profiles when averaged across all cases (note

the unfilled circles overlaid in Figs. 2b,c), however, are very much in agreement with MOST.

Last, the tower-based observations of ϕ_m at 6.5 m AGL are presented in Fig. 5a. Over 95% of ϕ_m values are in the 0.5–1.25 range. Given expected errors in the calculations of up to ~ 0.25 (see the appendix), the observations of near-surface vertical wind shear are also in good agreement with MOST predictions, which would be in the range of ≈ 0.6 –1 at a height of 6.5 m AGL for L ranging from -10 m to $-\infty$.

b. VORTEX-SE operations days in the prestorm and near-storm environments

The prestorm and near-storm environments (i.e., not within cool convective outflow) of VORTEX-SE operations days potentially differ from fair-weather days in that the former environments typically would be characterized by larger horizontal pressure-gradient forces and larger mean wind shear (the presence of larger mean shear is evident in Fig. 6a). On these days, the characteristics of the Doppler lidar-retrieved wind profiles exhibit significant departures from MOST with regularity. Considerably more shear is present than MOST would predict, as is evident in both the vertical profile of \bar{u}/u_* (Fig. 6b) and in ϕ_m (Fig. 6c). With respect to the latter, nearly 75% of the wind profiles are characterized by $\phi_m > 1$ in the surface layer (Fig. 6d).

Although MOST predictions of the profiles of \bar{u}/u_* and ϕ_m require consideration of the static stability, which is unknown at the location of CLAMPS, it is implausible to expect that these environments generally would be statically stable. In other words, even though there is uncertainty in the MOST prediction of \bar{u}/u_* and ϕ_m given the lack of knowledge of L at the CLAMPS site, MOST would not predict the slope of the \bar{u}/u_* profile to exceed k (Fig. 6b), and ϕ_m not to exceed 1 (Fig. 6c), given that these environments, like the fair-weather environments, would tend to be unstable or neutral (i.e., $L \leq 0$). Although the NOAA/ARL/ATDD towers are not collocated with CLAMPS, L indeed tends to be ≤ 0 within the prestorm and near-storm environments sampled at the towers (Figs. 4c,d). It is possible that some near-storm environments shaded by thunderstorm anvils (Markowski et al. 1998; Frame and Markowski 2010; Oberthaler and Markowski 2013) might have slightly stable surface layers ($L > 0$), in which case MOST would predict $\phi_m > 1$. However, the number of likely instances (only $\sim 10\%$ of the tower observations in this weather regime have $L > 0$; Figs. 4c,d) probably cannot account for the large fraction of surface-layer wind profiles in Fig. 6 exhibiting $\phi_m > 1$.

The tower-based observations of vertical wind shear just above the surface in prestorm and near-storm

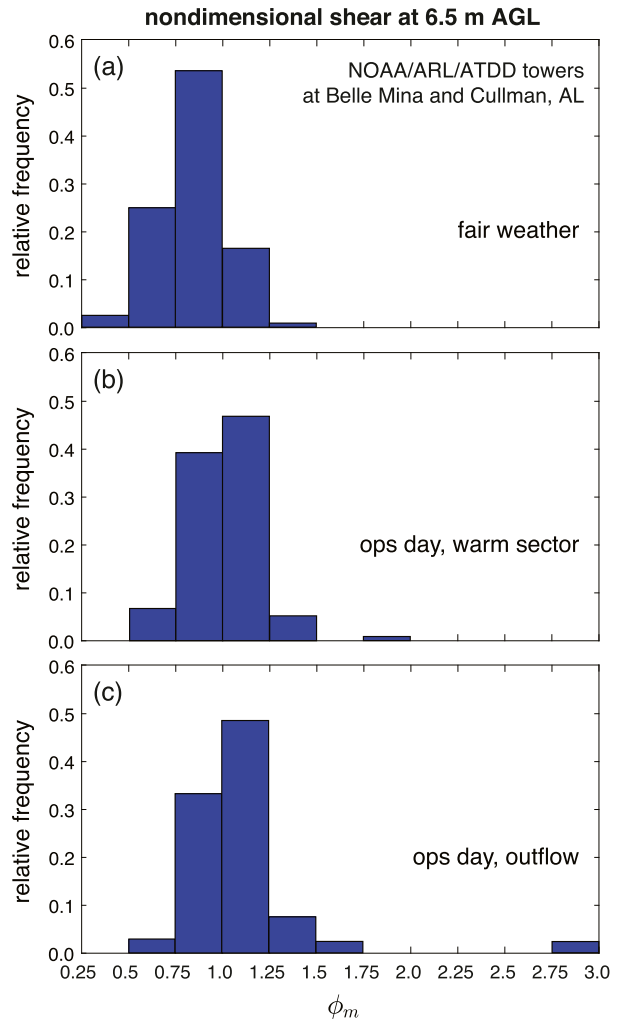


FIG. 5. Histograms of ϕ_m values at 6.5 m AGL for the various weather regimes, as diagnosed from the NOAA/ARL/ATDD tower observations at 3 and 10 m AGL.

environments also frequently exhibit departures from MOST expectations (Fig. 5b). Slightly more than 50% of the ϕ_m values measured in this weather regime exceed 1. Except in cases of strong surface-layer stabilization owing to cloud-shading effects, MOST predictions of ϕ_m would be in the 0.9–1.0 range (e.g., Businger et al. 1971).

c. VORTEX-SE operations days in the outflow of convective storms

The Doppler lidar-retrieved vertical wind profiles exhibit their largest departures from log-law behavior within convective outflow, where it seems that “almost anything goes” with respect to the characteristics of the wind profiles (Fig. 7). The variability is reminiscent of tower and radar observations of wind profiles within convective outflow made near Lubbock, Texas, by

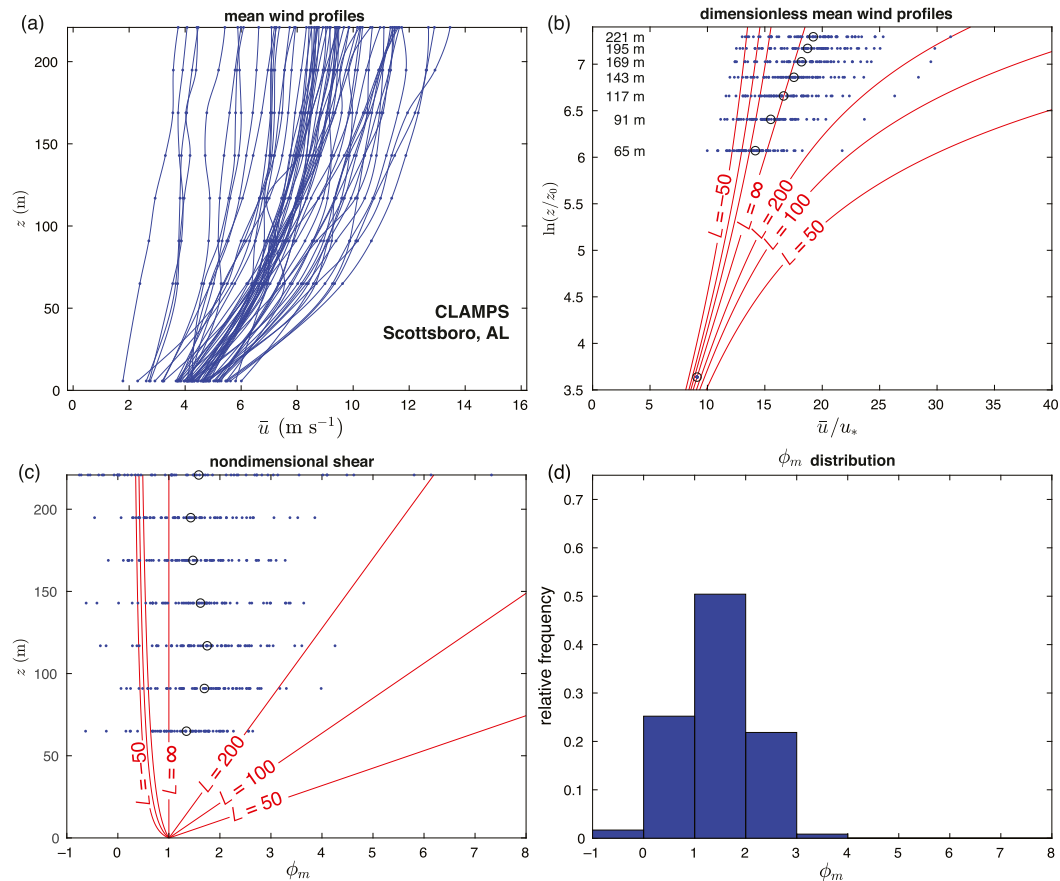


FIG. 6. As in Fig. 2, but for VORTEX-SE operations days before the arrival of convective storm outflow.

Lombardo et al. (2014) and Gunter and Schroeder (2015). At the lowest two lidar levels used (65 and 91 m AGL), ϕ_m values range from 0.5 to 6.8 (Figs. 7c,d). Admittedly, it is difficult to quantify the departures from MOST given the shortness of the averaging period (only 15-min averages are used within the outflow, as explained in section 2b), uncertainty in the depth of the surface layer, and uncertainty in the surface heat flux [negative surface heat fluxes are likely (Figs. 4e,f), for which $\phi_m > 1$ would be expected]. It seems unlikely that MOST could account for such variability, nor would MOST be expected to, given the likelihood of extreme unsteadiness and large horizontal heterogeneity. Regarding the MOST predictions for $L > 0$ in Figs. 7b,c, some words of caution are warranted. The corrections for a stable surface layer made in prior studies may not be applicable to the outflow of convective storms. Moreover, a *positive* surface heat flux is occasionally observed within thunderstorm outflow (12% of the time at the NOAA/ARL/ATDD tower sites; Fig. 4e).

The tower observations of vertical wind shear within convective outflow (Fig. 5c) also are more variable than

in fair-weather regimes or in the prestorm/near-storm environment (Figs. 5a,b), though not as variable as at the higher altitudes measured by the CLAMPS Doppler lidar. This is unsurprising given that MOST predicts ϕ_m to depart from unity by a term proportional to z/L . Although little can be said about the magnitude of the departures from MOST for the reasons given in the preceding paragraph, a stability-corrected ϕ_m value would be larger than unity in the case of $L > 0$.

4. Discussion

In addition to the surface-layer vertical shear, the friction velocity also is of interest given that surface stress is proportional to $-u_*^2$, and the surface stress is what typically must be parameterized in a numerical model. Models that parameterize this poorly probably cannot be expected to routinely predict the surface-layer vertical wind profiles accurately. Although MOST-based diagnoses of u_* (i.e., diagnoses of u_* from the wind immediately adjacent to the surface and the roughness length) generally were found not to depart

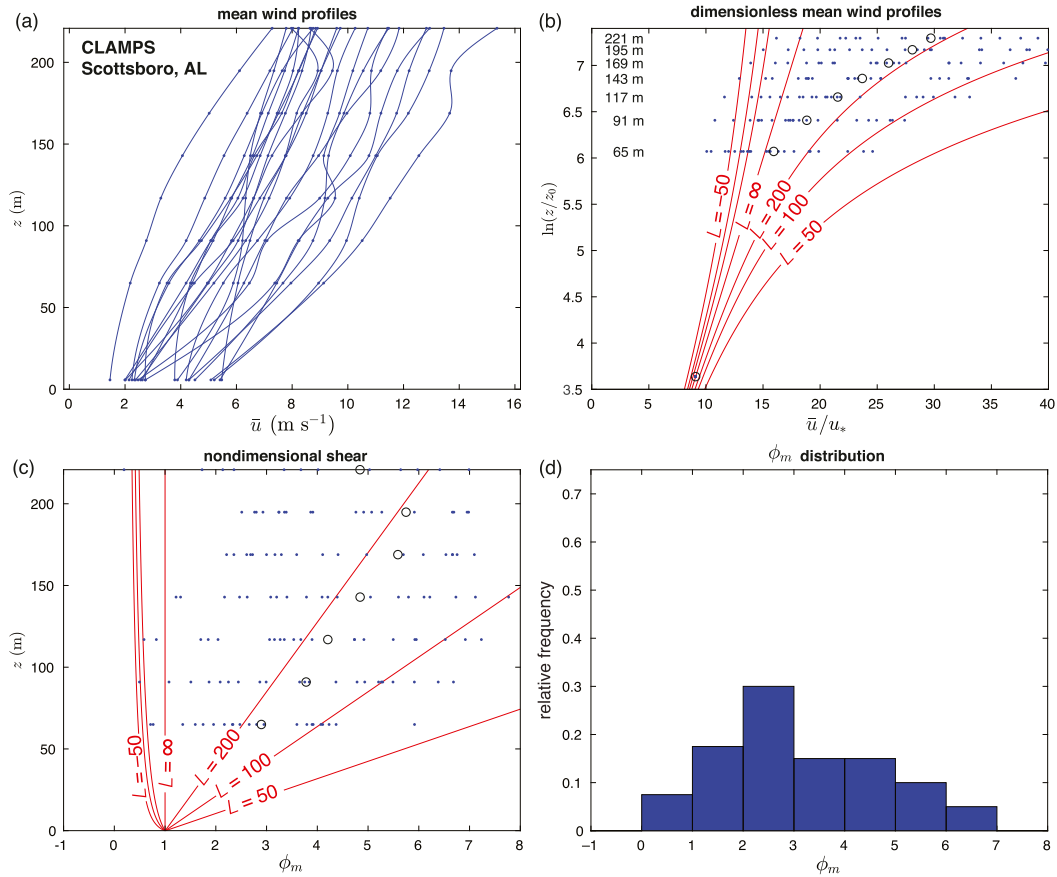


FIG. 7. As in Fig. 2, but within the outflow of convective storms occurring on VORTEX-SE operations days.

significantly from u_* values obtained from tower flux observations (Fig. 3), differences between MOST-based and tower-derived u_* values, which we might regard as errors in MOST-based u_* (and therefore surface stress), tend to be larger on thunderstorm days than on fair-weather days (Fig. 3). Moreover, the differences increase with increasing u_* (in Fig. 3, note the increasing distances between the dots and diagonal line as u_* increases). For the largest u_* values ($> \sim 0.5 \text{ m s}^{-1}$)—that is, when near-surface wind speeds are greatest—MOST-based u_* values are consistently too small, especially within convective outflow. This implies that a numerical simulation relying on a MOST-based lower boundary condition would have too little shear stress at the lower boundary. The use of stability-dependent drag coefficients does not address the fundamental problem, not only because the empirical relations are unlikely to apply to thunderstorms (they are derived from field experiments performed almost exclusively in “fair weather”), but also because a logarithmic behavior of the vertical wind profile is still assumed. One other issue with numerical simulations, especially those performed in the convective storms

community—from the idealized, research-driven simulations to the convection-allowing models (CAMs) now commonly relied upon for numerical weather prediction—is that the lower boundary condition is virtually always based on the instantaneous wind adjacent to the surface, as opposed to a temporally or spatially averaged wind.

The frequently large differences between the observed vertical wind shear and MOST-based predictions of vertical wind shear within the surface layer imply that numerical simulations, which virtually always assume the applicability of MOST in the formulation of the lower boundary condition (at least those simulations not assuming a free-slip lower boundary), are likely to have errors in their lower boundary condition and near-surface vertical wind profiles. On one hand, given the common observations of stronger shear than MOST predicts near and within convective storms, it would be tempting to conclude that numerical simulations using a MOST-based lower boundary condition would tend to underpredict surface-layer wind shear. On the other hand, many numerical simulations of storms, specifically those run

as large-eddy simulations (LES), might suffer from the problem exposed by [Markowski and Bryan \(2016\)](#), hereafter [MB16](#)).

[MB16](#) found that unrealistically large vertical wind shear develops, at least in boundary layers that are approximately statistically steady and horizontally homogeneous (i.e., boundary layers for which MOST is applicable), if the LES lacks significant, resolvable, turbulent eddies—not merely as the surface is approached, but throughout the entire depth of the domain. The “eddyless LES” problem [MB16](#) identified leads to even larger wind shear errors than the so-called log-layer-mismatch or law-of-the-wall problem in LES. The latter has been studied for decades (e.g., [Mason and Thomson 1992](#); [Sullivan et al. 1994](#); [Brasseur and Wei 2010](#)) and stems from inadequate resolution of turbulent eddies in the immediate vicinity of the surface (eddy size scales with distance above the surface).

[MB16](#) did not investigate environments in which significant departures from MOST might be present. That is, their work did not address the ability of an LES using a MOST-based lower boundary condition to correctly represent near-surface wind profiles in situations in which MOST does not apply in the first place.² However, this issue is raised here because both the MOST-based formulation of the lower boundary condition and the aforementioned problems with LES potentially can contribute to low-altitude wind shear errors in numerical simulations. From the analyses in [section 3](#), we can say with confidence that a MOST-based lower boundary condition is likely to be a source of model error in convective storm simulations. However, it is difficult to say what the range of adverse effects might include, given that “adverse effects” would be measured relative to past storm simulations, and some past simulations also might be affected by the issue identified by [MB16](#).

5. Summary and conclusions

The purpose of this article was to assess how closely surface-layer wind characteristics, vertical shear and surface shear stress in particular, agree with predictions

by MOST near and within convective storms. Departures from MOST within convective storm outflow were detectable in the Doppler lidar–based wind profiles, as well as in the micrometeorological tower data. Specifically, on thunderstorm days the vertical wind shear within the surface layer tended to be stronger than MOST predicts, both within the warm-sector air mass and within the convective outflow. This should not be surprising, given that MOST is based on the assumption of horizontal homogeneity and steadiness within a constant-flux surface layer. The atmosphere ahead of and within convective storms is not generally horizontal homogeneous and steady, rather, it is frequently characterized by strong horizontal temperature and pressure gradients and unsteadiness, especially near thunderstorm gust fronts.

It seems safe to conclude that a lower boundary condition based on MOST would be a source of error in numerical simulations of convective storms, given that many convective storm hazards and their parent storms are well known to be sensitive to the low-altitude vertical wind shear. It is unlikely that the community’s “first-order” understanding would be changed by improving the wall models used in convective storm simulations (i.e., the lower boundary condition and parameterization of near-surface turbulence). However, improvements in wall models—specifically, migrating to models that do not rely on the applicability of MOST ([Piomelli 2008](#))—are very likely to have a significant effect on the development of small-scale vortices (including tornadoes), vorticity budgets, low-altitude updrafts and downdrafts, and the transient momentum surges within the outflow that some have linked to tornado formation ([Lee et al. 2004](#); [Finley and Lee 2004](#); [Marquis et al. 2008](#); [Mashiko et al. 2009](#); [Wurman et al. 2010](#); [Kosiba et al. 2013](#); [Schenkman et al. 2014, 2016](#)). As numerical simulations continue moving toward higher and higher resolution (e.g., [Orf et al. 2017](#)), the near-surface flow will become better and better resolved, and surface interactions will need to be included in simulations in a better way.

Acknowledgments. We thank NOAA and all of the VORTEX-SE PIs, students, and other participants, without which the project would not have been possible. The analysis was supported by NOAA award NA17OAR4590189. Special thanks go to Ying Pan for extended discussions on this topic and her comments on the first draft of the manuscript. Marcelo Chamecki, Evgeni Fedorovich, Petra Klein, and Scott Salesky are also acknowledged for discussions related to this work.

²We cannot refute the possibility that a simulation using a MOST-based lower boundary condition, even though MOST might not be applicable, along with the simulation being run as an LES yet not resolving turbulent eddies—i.e., a model with two “wrongs”—could be better than a simulation with only one “wrong.” In the [MB16](#) “eddyless LES,” a MOST-based lower boundary condition was justified, but the LES contained no eddies.

Lastly, we appreciate the constructive and thorough critiques provided by the reviewers.

APPENDIX

Error Analysis for Friction Velocity, Dimensionless Velocity, and Dimensionless Shear

This appendix contains estimates of the errors in u_* , \bar{u}/u_* , and ϕ_m obtained from the CLAMPS observations, as well as estimates of the errors in measured and MOST-predicted u_* obtained from the NOAA/ARL/ATDD tower observations. The quantities derived from the CLAMPS observations are sensitive to errors in the Doppler lidar retrievals, anemometer winds, and the assumed z_0 , whereas the quantities derived from the tower observations are sensitive to errors in momentum fluxes, anemometer winds, and the assumed z_0 .

$$\delta u_* = \left[\left(\frac{\partial u_*}{\partial \bar{u}_a} \delta \bar{u}_a \right)^2 + \left(\frac{\partial u_*}{\partial z_0} \delta z_0 \right)^2 + \varepsilon^2 \right]^{1/2} = \left(\left\{ \frac{k}{\ln(z_a/z_0)} \delta \bar{u}_a \right\}^2 + \left\{ \frac{\bar{u}_a k}{[\ln(z_a/z_0)]^2 z_0} \delta z_0 \right\}^2 + \varepsilon^2 \right)^{1/2}, \quad (\text{A1})$$

where δu_* is the uncertainty in u_* , $\delta \bar{u}_a$ is the uncertainty in \bar{u}_a , δz_0 is the uncertainty in the assumed roughness length, and ε is the uncertainty in the applicability of (2).

Although the uncertainty in \bar{u}_a is often estimated as $\delta \bar{u}_a = \delta u_a / \sqrt{N}$, where δu_a is the uncertainty in each anemometer velocity observation and N is the number of observations used to compute the mean anemometer wind ($N = 361$ in the case of 30-min averages), the standard error is known to significantly underestimate the uncertainty because of the dependence between samples (Leith 1973; Wilks 2011). Mahrt and Thomas (2016) computed a modified standard error that was 2–3 times larger than the estimated uncertainty. For $\delta u_a = 0.3 \text{ m s}^{-1}$ per the manufacturer's specifications, a conservative estimate of $\delta \bar{u}_a$ that is three times the standard error is 0.05 m s^{-1} . This estimate, along with $z_a = 5.7 \text{ m}$, $z_0 = 0.15 \text{ m}$, and $\delta z_0 = 0.05 \text{ m}$ (section 2a), and an estimate of ε as the rms difference between measured and diagnosed u_* values at the location of the NOAA/ARL/ATDD towers (section 2b; Fig. 3), that is, $\varepsilon = 0.05 \text{ m s}^{-1}$, gives

$$\delta u_* = \left[(0.005 \text{ m s}^{-1})^2 + (0.09 u_*)^2 + (0.05 \text{ m s}^{-1})^2 \right]^{1/2}, \quad (\text{A2})$$

which is plotted in Fig. A1. For a diagnosed u_* ranging from 0.0 to 0.8 m s^{-1} , δu_* ranges from 0.05 to 0.09 m s^{-1} .

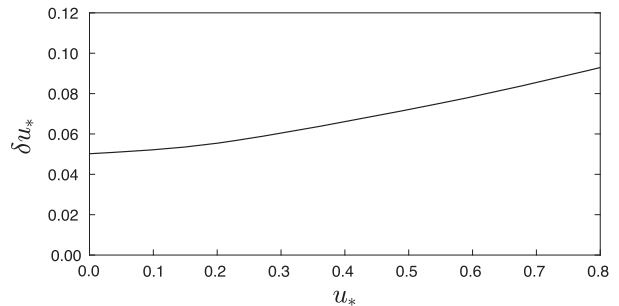


FIG. A1. Uncertainty in friction velocity, δu_* , diagnosed from MOST, at the CLAMPS deployment location.

a. u_* errors

Estimates of u_* obtained at the CLAMPS deployment location are not only prone to errors in \bar{u}_a and the assumed z_0 , but also to errors in the use of (2), which neglects the surface heat flux and assumes that MOST holds (section 2a). The uncertainty in u_* can be expressed as

At the NOAA/ARL/ATDD tower, u_* is computed via (3) (section 2b). The uncertainty in u_* is

$$\begin{aligned} \delta u_* &= \left[\left(\frac{\partial u_*}{\partial \overline{u'w'}} \delta \overline{u'w'} \right)^2 + \left(\frac{\partial u_*}{\partial \overline{v'w'}} \delta \overline{v'w'} \right)^2 \right]^{1/2} \\ &= \left[\left(\frac{1}{2} |\overline{u'w'}|^{-1/2} \delta \overline{u'w'} \right)^2 + \left(\frac{1}{2} |\overline{v'w'}|^{-1/2} \delta \overline{v'w'} \right)^2 \right]^{1/2}, \end{aligned} \quad (\text{A3})$$

where $\delta \overline{u'w'}$ and $\delta \overline{v'w'}$ are the uncertainties in the streamwise and crosswise vertical momentum fluxes, respectively. Neglecting the crosswise vertical momentum flux, which would be much smaller than the streamwise vertical momentum flux, (A3) becomes

$$\delta u_* = \frac{1}{2} |\overline{u'w'}|^{-1/2} \delta \overline{u'w'}. \quad (\text{A4})$$

From the manufacturer specifications, $\delta \overline{u'w'}$ is estimated to be $0.014 \text{ m}^2 \text{ s}^{-2}$. For $\overline{u'w'} = 0.01 \text{ m}^2 \text{ s}^{-1}$, the uncertainty in u_* measured by the NOAA/ARL/ATDD tower is $\delta u_* = 0.07 \text{ m s}^{-1}$.

b. \bar{u}/u_* errors

The uncertainty in \bar{u}/u_* is

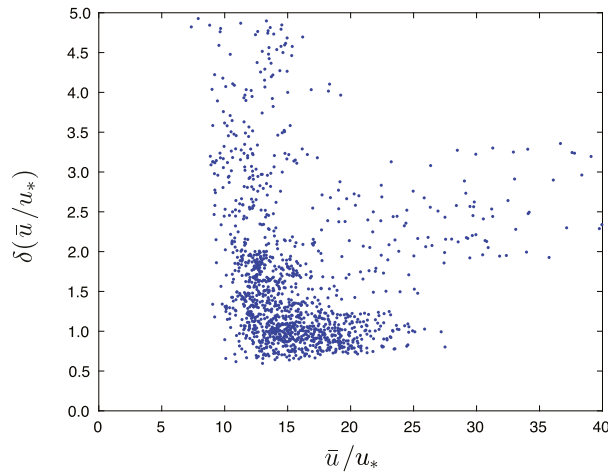


FIG. A2. Uncertainty in nondimensional velocity measured by the CLAMPS Doppler lidar, $\delta(\bar{u}/u_*)$, as a function of \bar{u}/u_* .

$$\begin{aligned} \delta(\bar{u}/u_*) &= \left[\left(\frac{\partial \bar{u} u_*^{-1}}{\partial \bar{u}} \delta \bar{u} \right)^2 + \left(\frac{\partial \bar{u} u_*^{-1}}{\partial u_*} \delta u_* \right)^2 \right]^{1/2} \\ &= \left[\left(\frac{\ln(z_a/z_0)}{\bar{u}_a k} \delta \bar{u} \right)^2 + \left(-\frac{\bar{u}}{u_*^2} \delta u_* \right)^2 \right]^{1/2} \\ &= \left[\left(\frac{\delta \bar{u}}{u_*^2} \right)^2 + \left(\frac{\bar{u} \delta u_*}{u_*^2} \right)^2 \right]^{1/2}. \end{aligned} \quad (\text{A5})$$

The standard error in the mean wind measured by the CLAMPS Doppler lidar is $\delta u/\sqrt{N}$, where $N = 11$ is the number of lidar wind observations made in a 30-min period ($N = 6$ for the 15-min averaging periods in convective storm outflow) and $\delta u = 0.5 \text{ m s}^{-1}$ is the uncertainty in each lidar-based wind measurement. A conservative estimate of $\delta \bar{u}$ that is twice the standard error yields $\delta \bar{u} = 0.3 \text{ m s}^{-1}$ for 30-min averages (0.4 m s^{-1} for 15-min averages).

Using the expression for δu_* in (A2) and $\delta \bar{u} = 0.3 \text{ m s}^{-1}$, Fig. A2 plots $\delta(\bar{u}/u_*)$ as a function of \bar{u}/u_* for all of the Doppler lidar-based wind observations. The uncertainty in $\delta(\bar{u}/u_*)$ is generally 0.7–2.0, though larger uncertainty is not unusual, depending on the characteristics of a particular wind profile.

c. ϕ_m errors

If ϕ_m is computed via

$$\phi_m = \frac{kz \Delta \bar{u}}{u_* \Delta z}, \quad (\text{A6})$$

where $\Delta \bar{u}/\Delta z$ is a finite-difference representation of $\partial \bar{u}/\partial z$, then the uncertainty in ϕ_m is

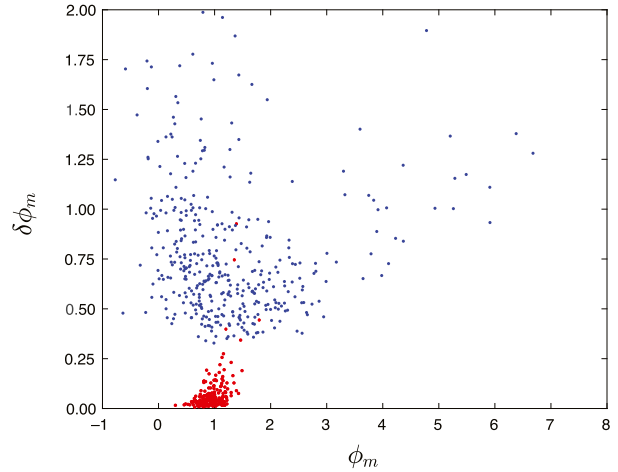


FIG. A3. Uncertainty in nondimensional shear $\delta \phi_m$ as a function of ϕ_m . Blue dots are for the CLAMPS Doppler lidar. Red dots are for the NOAA/ARL/ATDD tower.

$$\delta \phi_m = \left[\left(\frac{\partial \phi_m}{\partial \Delta \bar{u}} \delta \Delta \bar{u} \right)^2 + \left(\frac{\partial \phi_m}{\partial u_*} \delta u_* \right)^2 \right]^{1/2}, \quad (\text{A7})$$

$$= \left[\left(\frac{kz}{u_* \Delta z} \delta \Delta \bar{u} \right)^2 + \left(-\frac{\phi_m}{u_*} \delta u_* \right)^2 \right]^{1/2}, \quad (\text{A8})$$

where $\delta \Delta \bar{u} = \sqrt{2} \delta \bar{u}$ is the uncertainty in the wind speed differential measured between adjacent altitudes by the CLAMPS Doppler lidar or the NOAA/ARL/ATDD tower.

Figure A3 (blue dots) plots $\delta \phi_m$ for each Doppler lidar wind profile using $\delta \bar{u} = 0.3 - 0.4 \text{ m s}^{-1}$ (appendix section b), $\Delta z = 52 \text{ m}$ (vertical levels are 26 m apart, but centered-in-space finite-difference approximations are used except at the first lidar level), and the expression for δu_* given in (A2). For $\phi_m \sim 1$, $\delta \phi_m \sim 0.4 - 0.8$ in most situations. As is the case for $\delta(\bar{u}/u_*)$, larger uncertainty is possible, depending on the characteristics of a particular wind profile.

Figure A3 (red dots) also plots $\delta \phi_m$ for the NOAA/ARL/ATDD tower using $z = 6.5 \text{ m}$, $\Delta z = 7 \text{ m}$ (wind observations are at 3 and 10 m AGL), $\delta u_* = 0.7 \text{ m s}^{-1}$ (appendix section a), and $\delta \Delta u = \sqrt{2} \delta \bar{u} = \sqrt{2} (0.05 \text{ m s}^{-1}) = 0.07 \text{ m s}^{-1}$ ($\delta \bar{u}$ is similar for both the CLAMPS anemometer and tower anemometers). In the vast majority of situations, $\delta \phi_m \leq 0.25$.

REFERENCES

- Adlerman, E. J., and K. K. Droegemeier, 2002: The sensitivity of numerically simulated cyclic mesocyclogenesis to variations in model physical and computational parameters. *Mon. Wea. Rev.*, **130**, 2671–2691, [https://doi.org/10.1175/1520-0493\(2002\)130<2671:TSONSC>2.0.CO;2](https://doi.org/10.1175/1520-0493(2002)130<2671:TSONSC>2.0.CO;2).

- , —, and R. P. Davies-Jones, 1999: A numerical simulation of cyclic mesocyclogenesis. *J. Atmos. Sci.*, **56**, 2045–2069, [https://doi.org/10.1175/1520-0469\(1999\)056<2045:ANSOCM>2.0.CO;2](https://doi.org/10.1175/1520-0469(1999)056<2045:ANSOCM>2.0.CO;2).
- Brasseur, J., and T. Wei, 2010: Designing large-eddy simulation of the turbulent boundary layer to capture law-of-the-wall scaling. *Phys. Fluids*, **22**, 021303, <https://doi.org/10.1063/1.3319073>.
- Businger, J. A., J. C. Wyngaard, Y. Izumi, and E. F. Bradley, 1971: Flux-profile relationships in the atmospheric surface layer. *J. Atmos. Sci.*, **28**, 181–189, [https://doi.org/10.1175/1520-0469\(1971\)028<0181:FPRITA>2.0.CO;2](https://doi.org/10.1175/1520-0469(1971)028<0181:FPRITA>2.0.CO;2).
- Byun, D. W., 1990: On the analytical solutions of flux-profile relationships for the atmospheric surface layer. *J. Appl. Meteor.*, **29**, 652–657, [https://doi.org/10.1175/1520-0450\(1990\)029<0652:OTASOF>2.0.CO;2](https://doi.org/10.1175/1520-0450(1990)029<0652:OTASOF>2.0.CO;2).
- Coffer, B. E., and M. D. Parker, 2015: Impacts of increasing low-level shear on supercells during the early evening transition. *Mon. Wea. Rev.*, **143**, 1945–1969, <https://doi.org/10.1175/MWR-D-14-00328.1>.
- , and —, 2017: Simulated supercells in nontornadic and tornadic VORTEX2 environments. *Mon. Wea. Rev.*, **145**, 149–180, <https://doi.org/10.1175/MWR-D-16-0226.1>.
- , and —, 2018: Is there a “tipping point” between simulated nontornadic and tornadic supercells in VORTEX2 environments? *Mon. Wea. Rev.*, **146**, 2667–2693, <https://doi.org/10.1175/MWR-D-18-0050.1>.
- , —, J. M. L. Dahl, L. J. Wicker, and A. J. Clark, 2017: Volatility of tornadogenesis: An ensemble of simulated nontornadic and tornadic supercells in VORTEX2 environments. *Mon. Wea. Rev.*, **145**, 4605–4625, <https://doi.org/10.1175/MWR-D-17-0152.1>.
- Finley, C. A., and B. D. Lee, 2004: High resolution mobile mesonet observations of RFD surges in the June 9 Basset, Nebraska supercell during Project ANSWERS 2003. *22nd Conf. on Severe Local Storms*, Hyannis, MA, Amer. Meteor. Soc., P11.3, https://ams.confex.com/ams/11aram22sls/techprogram/paper_82005.htm.
- Foken, T., 2006: 50 years of the Monin–Obukhov similarity theory. *Bound.-Layer Meteor.*, **119**, 431–447, <https://doi.org/10.1007/s10546-006-9048-6>.
- Frame, J., and P. M. Markowski, 2010: Numerical simulations of radiative cooling beneath the anvils of supercell thunderstorms. *Mon. Wea. Rev.*, **138**, 3024–3047, <https://doi.org/10.1175/2010MWR3177.1>.
- , and —, 2013: Dynamical influences of anvil shading on simulated supercell thunderstorms. *Mon. Wea. Rev.*, **141**, 2802–2820, <https://doi.org/10.1175/MWR-D-12-00146.1>.
- Gibbs, J. A., E. Federovich, and A. Shapiro, 2015: Revisiting surface heat-flux and temperature boundary conditions in models of stably stratified boundary-layer flows. *Bound.-Layer Meteor.*, **154**, 171–187, <https://doi.org/10.1007/s10546-014-9970-y>.
- Gunter, W. S., and J. L. Schroeder, 2015: High-resolution full-scale measurements of thunderstorm outflow winds. *J. Wind Eng. Ind. Aerodyn.*, **138**, 13–26, <https://doi.org/10.1016/j.jweia.2014.12.005>.
- Högström, U., 1988: Non-dimensional wind and temperature profiles in the atmospheric surface layer. *Bound.-Layer Meteor.*, **42**, 55–78, <https://doi.org/10.1007/BF00119875>.
- Kosiba, K., J. Wurman, Y. Richardson, P. Markowski, P. Robinson, and J. Marquis, 2013: Genesis of the Goshen County, Wyoming, tornado (5 June 2009). *Mon. Wea. Rev.*, **141**, 1157–1181, <https://doi.org/10.1175/MWR-D-12-00056.1>.
- Lawson, J. R., J. S. Kain, N. Yussouf, D. C. Dowell, D. M. Wheatley, K. H. Knopfmeier, and T. A. Jones, 2018: Advancing from convection-allowing NWP to warn-on-forecast: Evidence of progress. *Wea. Forecasting*, **33**, 599–607, <https://doi.org/10.1175/WAF-D-17-0145.1>.
- Lee, B. D., C. A. Finley, and P. Skinner, 2004: Thermodynamic and kinematic analysis of multiple RFD surges for the 24 June 2003 Manchester, SD cyclic tornadic supercell during Project ANSWERS 2003. *22nd Conf. on Severe Local Storms*, Hyannis, MA, Amer. Meteor. Soc., P11.2, https://ams.confex.com/ams/11aram22sls/techprogram/paper_82000.htm.
- Lee, T. R., M. Buban, and T. Meyers, 2017: NOAA/ARL/ATDD micrometeorological tower data, version 1.0. UCAR/NCAR–Earth Observing Laboratory, accessed 15 January 2018, <https://doi.org/10.5065/D6TT4PPD>.
- , —, D. D. Turner, T. P. Meyers, and C. B. Baker, 2019: Evaluation of the High-Resolution Rapid Refresh (HRRR) model using near-surface meteorological and flux observations from Northern Alabama. *Wea. Forecasting*, **34**, 635–663, <https://doi.org/10.1175/WAF-D-18-0184.1>.
- Leith, C. E., 1973: The standard error of time-average estimates of climatic means. *J. Appl. Meteor.*, **12**, 1066–1069, [https://doi.org/10.1175/1520-0450\(1973\)012<1066:TSEOTA>2.0.CO;2](https://doi.org/10.1175/1520-0450(1973)012<1066:TSEOTA>2.0.CO;2).
- Lombardo, F. T., D. A. Smith, J. L. Schroeder, and K. C. Mehta, 2014: Thunderstorm characteristics of importance to wind engineering. *J. Wind Eng. Ind. Aerodyn.*, **125**, 121–132, <https://doi.org/10.1016/j.jweia.2013.12.004>.
- Mahrt, L., 1998: Stratified atmospheric boundary layers and breakdown of models. *Theor. Comput. Fluid Dyn.*, **11**, 263–279, <https://doi.org/10.1007/s001620050093>.
- , 1999: Stratified atmospheric boundary layers. *Bound.-Layer Meteor.*, **90**, 375–396, <https://doi.org/10.1023/A:1001765727956>.
- , 2010: Variability and maintenance of turbulence in the very stable boundary layer. *Bound.-Layer Meteor.*, **135**, 1–18, <https://doi.org/10.1007/s10546-009-9463-6>.
- , 2014: Stably stratified atmospheric boundary layers. *Annu. Rev. Fluid Mech.*, **46**, 23–45, <https://doi.org/10.1146/annurev-fluid-010313-141354>.
- , and C. K. Thomas, 2016: Surface stress with non-stationary weak winds and stable stratification. *Bound.-Layer Meteor.*, **159**, 3–21, <https://doi.org/10.1007/s10546-015-0111-z>.
- Markowski, P. M., 2016: An idealized numerical simulation investigation of the effects of surface drag on the development of near-surface vertical vorticity in supercell thunderstorms. *J. Atmos. Sci.*, **73**, 4349–4385, <https://doi.org/10.1175/JAS-D-16-0150.1>.
- , and Y. P. Richardson, 2014: The influence of environmental low-level shear and cold pools on tornadogenesis: Insights from idealized simulations. *J. Atmos. Sci.*, **71**, 243–275, <https://doi.org/10.1175/JAS-D-13-0159.1>.
- , and G. H. Bryan, 2016: LES of laminar flow in the PBL: A potential problem for convective storm simulations. *Mon. Wea. Rev.*, **144**, 1841–1850, <https://doi.org/10.1175/MWR-D-15-0439.1>.
- , E. N. Rasmussen, J. M. Straka, and D. C. Dowell, 1998: Observations of low-level baroclinity generated by anvil shadows. *Mon. Wea. Rev.*, **126**, 2942–2958, [https://doi.org/10.1175/1520-0493\(1998\)126<2942:OOLLBG>2.0.CO;2](https://doi.org/10.1175/1520-0493(1998)126<2942:OOLLBG>2.0.CO;2).
- Marquis, J. N., Y. P. Richardson, J. M. Wurman, and P. M. Markowski, 2008: Single- and dual-Doppler analysis of a tornadic vortex and surrounding storm scale flow in the Crowell, Texas, supercell of 30 April 2000. *Mon. Wea. Rev.*, **136**, 5017–5043, <https://doi.org/10.1175/2008MWR2442.1>.
- Mashiko, W., 2016: A numerical study of the 6 May 2012 Tsukuba City supercell tornado. Part II: Mechanisms of tornadogenesis.

- Mon. Wea. Rev.*, **144**, 3077–3098, <https://doi.org/10.1175/MWR-D-15-0122.1>.
- , H. Niino, and T. Kato, 2009: Numerical simulation of tornadogenesis in an outer-rainband minisupercell of Typhoon Shanshan on 17 September 2006. *Mon. Wea. Rev.*, **137**, 4238–4260, <https://doi.org/10.1175/2009MWR2959.1>.
- Mason, P. J., and D. J. Thomson, 1992: Stochastic backscatter in large-eddy simulations of boundary layers. *J. Fluid Mech.*, **242**, 51–78, <https://doi.org/10.1017/S0022112092002271>.
- Monin, A. S., and A. M. Obukhov, 1954: Osnovnye zakonomernosti turbulentnogo peremeshivaniya v prizemnom sloe atmosfery (Basic laws of turbulent mixing in the atmosphere near the ground). *Tr. Geofiz. Inst., Akad. Nauk SSSR*, **24**, 163–187. [A 1959 translation is available from Defense Technical Information Center (<http://handle.dtic.mil/100.2/AD672723>).]
- Nowotarski, C. J., and P. M. Markowski, 2016: Modifications to the near-storm environment induced by simulated supercell thunderstorms. *Mon. Wea. Rev.*, **144**, 273–293, <https://doi.org/10.1175/MWR-D-15-0247.1>.
- , —, Y. P. Richardson, and G. H. Bryan, 2014: Properties of a simulated convective boundary layer in an idealized supercell thunderstorm environment. *Mon. Wea. Rev.*, **142**, 3955–3976, <https://doi.org/10.1175/MWR-D-13-00349.1>.
- , —, —, and —, 2015: Supercell low-level mesocyclones in simulations with a sheared convective boundary layer. *Mon. Wea. Rev.*, **143**, 272–297, <https://doi.org/10.1175/MWR-D-14-00151.1>.
- Oberthaler, A. J., and P. M. Markowski, 2013: A numerical simulation study of the effects of cloud shading on quasilinear convective systems. *J. Atmos. Sci.*, **70**, 767–793, <https://doi.org/10.1175/JAS-D-12-0123.1>.
- Optis, M., A. Monahan, and F. C. Bosveld, 2014: Moving beyond Monin–Obukhov similarity theory in modelling wind-speed profiles in the lower atmospheric boundary layer under stable stratification. *Bound.-Layer Meteor.*, **153**, 497–514, <https://doi.org/10.1007/s10546-014-9953-z>.
- Orf, L., R. Wilhelmson, B. Lee, C. Finley, and A. Houston, 2017: Evolution of a long-track violent tornado within a simulated supercell. *Bull. Amer. Meteor. Soc.*, **98**, 45–68, <https://doi.org/10.1175/BAMS-D-15-00073.1>.
- Pan, Y., and E. G. Patton, 2017: On determining stationary periods within time series. *J. Atmos. Oceanic Technol.*, **34**, 2213–2232, <https://doi.org/10.1175/JTECH-D-17-0038.1>.
- Pearson, G., F. Davies, and C. Collier, 2009: An analysis of the performance of the UFAM pulsed Doppler lidar for observing the boundary layer. *J. Atmos. Oceanic Technol.*, **26**, 240–250, <https://doi.org/10.1175/2008JTECHA1128.1>.
- Piomelli, U., 2008: Wall-layer models for large-eddy simulations. *Prog. Aerosp. Sci.*, **44**, 437–446, <https://doi.org/10.1016/j.paerosci.2008.06.001>.
- Roberts, B., M. Xue, A. D. Schenkman, and D. T. Dawson II, 2016: The role of surface drag in tornadogenesis is within an idealized supercell simulation. *J. Atmos. Sci.*, **73**, 3371–3395, <https://doi.org/10.1175/JAS-D-15-0332.1>.
- Schenkman, A. D., M. Xue, and A. Shapiro, 2012: Tornadogenesis in a simulated mesovortex within a mesoscale convective system. *J. Atmos. Sci.*, **69**, 3372–3390, <https://doi.org/10.1175/JAS-D-12-038.1>.
- , —, and M. Hu, 2014: Tornadogenesis in a high-resolution simulation of the 8 May 2003 Oklahoma City supercell. *J. Atmos. Sci.*, **71**, 130–154, <https://doi.org/10.1175/JAS-D-13-073.1>.
- , —, and D. T. Dawson II, 2016: The cause of internal outflow surges in a high-resolution simulation of the 8 May 2003 Oklahoma City tornadic supercell. *J. Atmos. Sci.*, **73**, 353–370, <https://doi.org/10.1175/JAS-D-15-0112.1>.
- Stensrud, D. J., and Coauthors, 2009: Convective-scale warn-on-forecast system: A vision for 2020. *Bull. Amer. Meteor. Soc.*, **90**, 1487–1500, <https://doi.org/10.1175/2009BAMS2795.1>.
- Sullivan, P. P., J. C. McWilliams, and C.-H. Moeng, 1994: A subgrid-scale model for large-eddy simulation of planetary boundary-layer flows. *Bound.-Layer Meteor.*, **71**, 247–276, <https://doi.org/10.1007/BF00713741>.
- Turner, D., 2017: OU/NSSL CLAMPS Doppler lidar wind profile data, version 1.0. UCAR/NCAR–Earth Observing Laboratory, accessed 15 January 2018, <https://doi.org/10.5065/D6P55M7B>.
- , 2018: OU/NSSL CLAMPS surface meteorological data, version 2.0. UCAR/NCAR–Earth Observing Laboratory, accessed 15 January 2018, <https://doi.org/10.5065/D6DN43S8>.
- Wagner, T. J., P. M. Klein, and D. D. Turner, 2019: A new generation of ground-based mobile platforms for active and passive profiling of the boundary layer. *Bull. Amer. Meteor. Soc.*, **100**, 137–153, <https://doi.org/10.1175/BAMS-D-17-0165.1>.
- Wilks, D., 2011: *Statistical Methods in the Atmospheric Sciences*. 3rd ed. International Geophysics Series, Vol. 100, Academic Press, 704 pp.
- Wilson, J. D., 2008: Monin–Obukhov functions for standard deviations of velocity. *Bound.-Layer Meteor.*, **129**, 353–369, <https://doi.org/10.1007/s10546-008-9319-5>.
- Wurman, J., K. A. Kosiba, P. Markowski, Y. Richardson, D. Dowell, and P. Robinson, 2010: Finescale and dual-Doppler analysis of tornado intensification, maintenance, and dissipation in the Orleans, Nebraska, tornadic supercell. *Mon. Wea. Rev.*, **138**, 4439–4455, <https://doi.org/10.1175/2010MWR3330.1>.
- Yokota, S., H. Niino, H. Seko, M. Kunii, and H. Yamauchi, 2018: Important factors for tornadogenesis as revealed by high-resolution ensemble forecasts of the Tsukuba supercell tornado of 6 May 2012 in Japan. *Mon. Wea. Rev.*, **146**, 1109–1132, <https://doi.org/10.1175/MWR-D-17-0254.1>.